Environmental Science Nano

ROYAL SOCIETY OF CHEMISTRY

PAPER

View Article Online
View Journal | View Issue

Cite this: *Environ. Sci.: Nano*, 2025, **12**, 2309

Enhanced VOC recycling by nano-Fe/FeO$_x$ decorated nanoporous carbon†

Weiping Zhang, *[ab] Xiong Xiao,[ab] Xiaoqin Wang,[ab] Hongli Liu,[ab] Xingye Zeng[c] and Taicheng An [ab]

Received 8th January 2025,
Accepted 13th February 2025

DOI: 10.1039/d5en00019j

rsc.li/es-nano

The recycling of industrial VOCs has attracted enormous interest for its significant roles in mitigating VOC emissions and reducing human and environmental risks. Here, we report a highly efficient multifunctional Fe/FeO$_x$/NPC adsorbent, which shows high adsorption capacity for toluene (200 mg g^{-1}) and ethyl acetate (154 mg g^{-1}) and 100% regeneration efficiency without deactivation after five cycles. By introducing nano-Fe/FeO$_x$, the S_{BET} and pore volume of NPC are increased from 163.66 m^2 g^{-1} and 0.142 mL g^{-1} to 361.30 m^2 g^{-1} and 0.22 mL g^{-1}, respectively. It is achieved by a multifunctional adsorbent that provides efficient adsorption and thermal effect sites (Fe^0, FeO$_x$ and graphitic carbon), which cooperatively facilitates adsorption–regeneration. More significantly, the thermal effect sites and diverse pore structures play a crucial role in the successive and synergetic separation and desorption of VOCs from the multifunctional adsorbent. The thermal effect sites on Fe/FeO$_x$/NPC can effectively inhibit the conversion of the thermal activation reaction of VOCs into high-boiling carbonates, thereby avoiding the formation of heel build-up and deactivation of adsorbents. Our research introduces an efficient VOC recycling approach enabled by subtle control of VOC regeneration on a multifunctional interface.

Environmental significance

For recycling high-value VOCs, the big problem faced in VOC recycling is the deactivation of the adsorbents, which limits their application in the rapid demand for VOC resource utilization or control. In this study, we fabricated a multifunctional Fe/FeO$_x$/NPC adsorbent with 100% regeneration efficiency by a method of *in situ* carbon reconstruction. The adsorption and regeneration mechanism were revealed by *in situ* DRIFTS, infrared thermography and Spearman correlation. The enhanced adsorption and regeneration were mainly attributed to the diverse pore structures and abundant thermal effect sites. This is of great significance for the design of highly efficient and stable adsorbents by optimizing pore structure and active sites for VOC recycling and control.

1. Introduction

In the context of pollution and carbon reduction, the emission of highly concentrated volatile organic gas in the industrial production process not only brings serious environmental health hazards but also becomes a stumbling block restricting the development of enterprises.[1,2] Recently, numerous VOC abatement methods have been developed, including recycling methods such as adsorption,[3] absorption,[4] condensation,[5] and membrane separation[6] and destruction elimination methods such as catalytic oxidation,[7] photocatalytic oxidation,[8,9] and biological degradation.[10] Among them, adsorption technology based on porous carbon adsorption has been widely used in VOC pollution control for its economic features and sustainability advantages, especially in capturing highly toxic and value-added compounds from industrial VOCs exhaust.[2,11,12] However, the inefficient recovery of VOCs often brings high exhaust gas disposal costs during recycling and utilization. Therefore, research and development of carbon-based absorbents with highly stable and efficient VOC recovery is an urgent task to protect environmental sustainability and human health, and it

[a] *Guangdong Key Laboratory of Environmental Catalysis and Health Risk Control, Guangdong-Hong Kong-Macao Joint Laboratory for Contaminants Exposure and Health, Institute of Environmental and Chemical Engineering Innovation, Institute of Environmental Health and Pollution Control, Guangdong University of Technology, Guangzhou 510006, China. E-mail: wp.zhang86@gdut.edu.cn*
[b] *National Engineering Laboratory for VOCs Pollution Control Material & Technology Guangdong Branch, Guangdong Basic Research Center of Excellence for Ecological Security and Green Development, Guangdong Engineering Technology Research Centre for Photocatalytic Technology Integration and Equipment, School of Environmental Science and Engineering, Guangdong University of Technology, Guangzhou 510006, China*
[c] *School of Chemical Engineering, Guangdong University of Petrochemical Technology, Maoming, 525000, P. R. China*
† Electronic supplementary information (ESI) available. See DOI: https://doi.org/10.1039/d5en00019j

is also of great practical significance that VOCs are recycled to make it more in line with the dual carbon strategy.

Current studies have shown that the pore channels and structural characteristics of porous carbon adsorbents are decisive factors affecting VOCs' adsorption and mass transfer during the adsorption and desorption process.[13–15] Porous carbon adsorbents, such as activated carbon (AC), have the accessibility of micropores (<2 nm) and high specific surface area and pore volume, which can be used to recover most types of VOCs including aromatics, esters, alkanes, and aldehydes.[2,16,17] Ye *et al.* reported a microporous carbon prepared by hydrothermal carbonization coupled with chemical activation, and the well-developed microporosity with an 81% enhancement could significantly improve the adsorption of ethyl acetate at low concentrations.[18] However, the rapid transfer of VOC molecules will block the micropores of AC and cause slower mass transfer and diffusion, leading to low desorption efficiency.[2,19] Many studies have shown that the mesoporous structure of carbon adsorbents can provide more efficient diffusion channels for the mass transfer of VOCs by reducing the spatial resistance.[20,21] Wang *et al.* found that the unusual bimodal-like pore size distribution of mesoporous carbon gave the adsorbates a higher diffusion rate compared with conventional adsorbents such as activated carbon and carbon molecular sieve.[22] The introduction of a mesoporous structure can significantly improve the diffusion channel of VOC molecules on porous carbon so that it has more efficient accessibility in the adsorption process and higher mass transfer diffusion efficiency in the resolution process.[21,23]

Although optimizing the pore structure can effectively promote the mass transfer and diffusion of VOC molecules, the incomplete desorption of VOCs often leads to the gradual deactivation of the adsorbent.[2,24] During thermal desorption, VOC molecules or VOCs and the adsorption interface may undergo thermal and chemical reactions, resulting in the formation of hard-to-separate polymeric species (heel build-up), ultimately leading to the progressive deactivation of the adsorbent.[25,26] In our previous study, the strong chemisorption between ethyl acetate molecules and adsorbents severely hampered the complete regeneration of the adsorbent. A large number of carbonaceous species such as 1,2-benzenedicarboxylic acid, dihexyl ester, and dioctyl phthalate were accumulated on adsorbents, which confirmed thermal chemical reactions between EA molecules or CBC defect sites to form high-boiling carbonaceous by-products.[15] Heel build-up was attributed to the formation of these heavier molecules trapped in or blocking the micropores.[27,28] Besides, adsorbed oxygen or oxygen-containing functional groups (OCFGs) can also increase heel build-up on AC due to the formation of chemical bonds between O_2/OCFG and adsorbate/adsorbent at high temperatures, leading to the loss of micropore sites through the formation of permanent heel species.[29,30] Therefore, the abundance of micropores and the scarcity of meso- and macropores may have increased heel formation due to mass diffusion resistance.[2,27]

Heel build-up on porous carbon adsorbents will shorten their lifetime by reducing their VOC uptake capacity. Several researchers have focused on inhibiting heel formation by operating parameters such as chemical modification,[31] regulating pore structure,[27] and regeneration condition.[30,32–34] Bhat reported an effective surface modification strategy with a 55% increase in porosity and effective functional groups, and the percentage of heel accumulation in surface-modified BAC is significantly lower (≤3%) compared to unmodified BAC.[35] Jahandar Lashaki *et al.* compared the contribution of the mesoporous structure of activated carbon to the adsorption and desorption behaviour of VOCs; the result showed that mesoporous BACs not only enhanced competitive adsorption kinetics but also yielded faster desorption of the adsorbed species.[36] Faster desorption kinetics would also shorten the duration of the regeneration step, which is particularly important to inhibit the thermal chemical reaction of VOCs at the interface. Interestingly, some research showed that the thermal chemical reaction of VOCs could be significantly inhibited by some transition metals, such as single atoms or oxide nanoclusters of Fe, Cu, and Ni, due to their high C–H activation energy barrier.[37,38] Meanwhile, its application to the coupling modification of adsorbents could effectively improve the regeneration efficiency of adsorbents.[39] To the best of our knowledge, no previous work has been done to inhibit or avoid heel accumulation *via* metal modification of porous carbon while maintaining high adsorption capacity.

In this paper, functional Fe–C composite adsorbents with high adsorption and regeneration properties were constructed by a method of nano-Fe-catalysed *in situ* carbon reconstruction, which aimed to control the skeleton structure and thermal effect site of porous carbon. Compared with traditional activated carbon, Fe–C composites have a more diversified hierarchical structure and metal sites, which not only provide more adsorption active sites for VOCs but also provide sufficient heat and mass transfer channels for the rapid diffusion of VOCs inside the adsorbents. In addition, thanks to the *in situ* thermal effect of nano-Fe/FeO_x, the heat transfer of VOCs in the porous carbon channel can be effectively promoted due to the enhancement of the thermal conductivity of the porous carbon adsorbents. Owing to abundant nano-Fe/FeO_x, the VOCs can be separated by electron transfer during thermal desorption, which greatly reduces the thermal activation reaction of VOCs on the adsorption interface, avoiding heel formation and deactivation of porous carbon adsorbents. The research can provide solid theoretical and technical support for the upgrading of resource recovery and adsorption control of industrial VOC waste gas.

2. Experimental section

2.1 Adsorbents preparation

Fe–C composite (Fe/FeO_x/NPC) adsorbents are prepared as follows. 5 g of sucrose and a certain amount of iron acetate were dissolved in 50 mL ethanol solution (V_{EtOH}/V_{water} = 1/4). Approximately 20 mL of bacterial cellulose (BC) dispersion

was added, and a relatively homogeneous colloidal dispersion was obtained by ultrasonically stirring and dispersing the pretreated mixture for 30 min at room temperature. Next, the above colloidal dispersion was transferred to a 100 mL reactor. Then the reaction was carried out hydrothermally in an oven at an elevated temperature rate of 10 °C min^{-1} to 180 °C for 6 h. A chocolate-brown product was obtained and collected by centrifugal washing with ethanol shaking 1–2 times, washed to neutrality with distilled water, and then subjected to the drying process. The dried products were placed in a tube furnace, heated to 400 °C at 5 °C min^{-1} for 4 h with argon gas protection, and then the temperature was increased to 500, 600, 750, 850 and 950 °C for 2 h, respectively. Finally, the Fe–C composite adsorbent was obtained and labelled as Fe–C-*X* (*X* = 500, 600, 750, 850, and 950). All of the chemical reagents used were analytical grade and received without further purification and the details can be seen in the ESI.†

2.2 Characterization

The morphology and interior structure of the adsorbent were observed using a transmission electron microscope (TEM, JEM-2100F, Japan). The N_2 adsorption–desorption isotherms and pore size distributions at 77 k were quantified using an ASAP 2020 PLUS HD88 surface area and porosity analyser (Micromeritics, USA). The thermal decomposition behaviour of the adsorbent was assessed by TG-DSC. The functional groups were identified using a Fourier-transform infrared (FT-IR) instrument in the wavenumber range of 2000–800 cm^{-1}. X-ray photoelectron spectroscopy (XPS, ESCALAB 250, Thermo Fisher) was used to analyse the composition and elemental chemical state of the samples. The chemical composition and molecular structure of the synthesized samples were analysed by UV laser Raman spectroscopy (HORIBA Jobin Yvon, France). The thermal effect of Fe–C adsorbents was analysed by an infrared thermal imager (FOTRIC 280). The species and adsorbed states of functional groups on the adsorbent surface were analysed using *in situ* diffuse reflectance infrared.

2.3 Determination of functional groups

The adsorbents possessed oxygen functionalities in the form of carboxylic, lactonic, phenolic, and basic groups, which could be quantitatively determined as previously reported.[15] To ensure titration precision, back-titration was adopted to reduce the impact of CO_2. For each analysis, 70 mg of adsorbents were added to 30 mL of 0.05 M $NaHCO_3$, NaOH, HCl, and 15 mL of 0.05 M Na_2CO_3 solution, respectively. The solutions were agitated for 24 h and then filtered and the filtrates were collected. The filtrates were acidified with excessive 0.05 M HCl. Then, the acidified solutions were purged with nitrogen to expel CO_2. The purge time was set from 120 to 180 min. After CO_2 expulsion, the solution was back-titrated with 0.05 M NaOH. A colour indicator of phenolphthalein was used for endpoint determination. For each adsorbent and reaction base, samples were tested in triplicate with a parallel blank reference. During titration, the blank sample was exposed to the same procedures that were applied to adsorbent samples. The final result was calculated with the averaged measurement minus the blank.

2.4 Adsorption, regeneration and semiquantitative analysis

Dynamic adsorption of toluene and EA was carried out using a GC-9800 gas chromatograph at room temperature, and the details of the evaluation of adsorption performance can be seen in the ESI.† The desorption procedure was conducted according to our previous report.[15] Prior to the desorption experiments, EA and toluene first reached adsorption equilibrium on the adsorbent. The Fe–C adsorbents were regenerated using a hot N_2 stream at 30 mL min^{-1}. N_2 was purged into the sample column at the start of regeneration, and the programmed warming mode was activated to heat up to 120 °C at a rate of 5 °C min^{-1}. The output EA and toluene concentrations were monitored online by GC, and the desorption process took 6 h. The adsorbent was then cooled to room temperature before being utilized in the next adsorption cycle. The adsorption/desorption tests were repeated five times. After multiple adsorption–desorption recycling, the composition and functional groups of Fe–C adsorbents were determined by an XPS semiquantitative analysis method.

2.5 *In situ* DRIFTS

EA and toluene adsorption on the synthesized adsorbents was recorded on a Thermo Scientific Nicolet iS10 Fourier-transform infrared spectrometer equipped with an MCT detector. Prior to each adsorption test, the adsorbent was loaded into a porous screen at the bottom of a Harrick Scientific Praying Mantis diffuse reflectance cell, which had two ZnSe windows and one glass observation window, and then the cell was sealed with a dome. After 20 min of nitrogen purging to remove the gas from the adsorption chamber, the sample was heated to 150 °C in a 30 mL min^{-1} N_2 flow for 120 min. After cooling to 30 °C, a background spectrum of the adsorbent was first obtained in the N_2 flow, followed by switching N_2 to ethyl acetate and toluene stream (30 mL min^{-1}) for the adsorption experiment. The signals of infrared information on the adsorbents surface were collected every 10 min for a total of 50 min. All DRIFT spectra were recorded at a resolution of 4 cm^{-1} in the range of 4000 to 400 cm^{-1}.

3. Results and discussion

3.1 Morphology and composition analysis

TEM analysis was carried out to estimate the lattice structure and distribution of nano-Fe. As shown in Fig. 1a, highly dispersed nanoclusters of Fe or its oxides were obtained by a method of *in situ* carbon reconstruction, and the formation of large oxide particles was also avoided. Fig. 1b and c show the HRTEM images of the Fe–C composite. The lattice spacing of 0.2 and 0.29 nm was observed, which could be attributed to the lattice structure of zero-valent iron (Fe^0) and the (311) Fe_3O_4.[40] The presence of Fe oxides at the boundary of

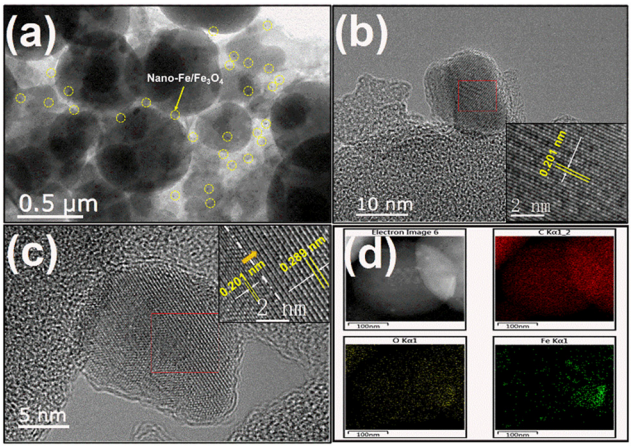

Fig. 1 TEM image (a), HRTEM images (b and c, the inset pictures are the lattice parameters of nano-iron components), and element mapping (d) of the prepared Fe–C composite.

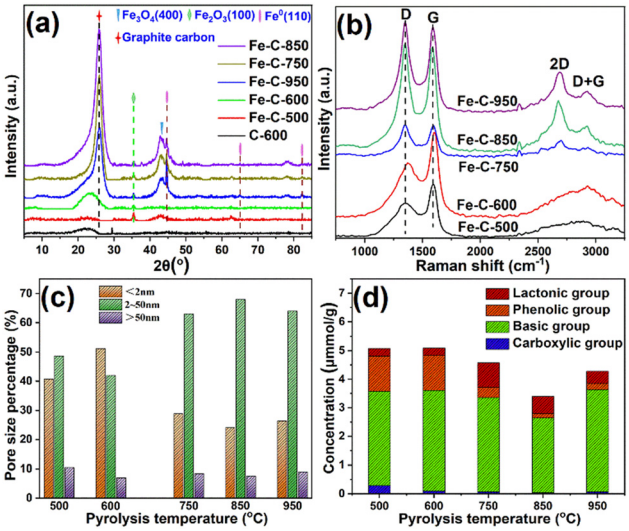

Fig. 2 XRD (a), Raman spectra (b), pore size percentage (c), and concentration of functional groups (d) in Fe–C composites prepared at different pyrolysis temperatures.

iron nanoparticles may be due to the fact that the ferric oxides are not completely reduced to Fe^0 during carbon reconfiguration. On the other hand, it may also be caused by local oxidation of the formed Fe^0. Meanwhile, the elemental mapping diagram (Fig. 1d) also confirmed the homogeneous distribution of elements C, O, and Fe in the Fe–C composite. These results displayed that Fe nanoparticles with high crystallinity are highly dispersed and closely coupled with carbon in the Fe–C complexes. Close contact between them tends to have stronger metallic bonding and a higher electron density, which may allow the material to have excellent thermal conductivity and coordination adsorption capacity, favouring heat transfer during the desorption process.[41]

3.2 Basic structure and functional group analysis

To elucidate the structure and properties of the material, the crystal structure of Fe–C composites was analysed by X-ray powder diffraction (XRD) and is shown in Fig. 2a. A characteristic peak of 2θ = 25.8° was observed from the spectra, which were assigned to the crystal faces (002) of graphitic carbon.[42] Two characteristic peaks observed at 2θ = 35.6° and 43.4° are assigned to the crystal faces (100) of Fe_2O_3 (PDF 98-000-0240) and the crystal faces (311) of Fe_3O_4 (PDF 98-000-0294).[39] The characteristic peak of Fe^0 was observed at 44.8°. These results are in agreement with the TEM analysis results. Typically, when the pyrolysis temperature was gradually increased, the intensity of graphitic carbon and the Fe^0 characteristic peak was significantly increased. In other words, the interfacial Fe–C composition has been significantly changed during the carbon reconstruction, and the graphitization degree of nanoporous carbon was significantly enhanced by nano-Fe, resulting in the optimization of the pore channel structure. A uniform nanostructure of Fe elements was formed in porous carbon, which caused more nano-Fe exposure and was very favourable for improving the coordination of metals for VOC adsorption.[43] Meanwhile, the enhanced graphitization of porous carbon is conducive to enhancing the π–π conjugation effect of the adsorbent and helps to improve its adsorption–desorption of VOCs.[2,44]

Raman spectroscopy was used to further validate the graphitized extent of the adsorbents. As shown in Fig. 2b, the two vibrational modes at 1340 cm^{-1} (D band) and 1590 cm^{-1} (G band) were assigned to the disordered structure of carbon and the planar stretching vibration of sp^2 hybridization.[45] The I_D/I_G of the tested Fe–C composites was calculated based on the deconvolution of Raman spectra. The lower the value of I_D/I_G, the higher the degree of graphitization of porous carbon.[15,46] With the increase of pyrolysis temperature, the I_D/I_G value gradually decreased to 1.41, and there was a rapid decrease from 600 °C to 750 °C, which suggested that high pyrolysis temperature helped to promote the graphitization of Fe–C adsorbents. However, when there was no nano-Fe in the porous carbon adsorbent, the I_D/I_G of C-850 adsorbent was as high as 2.70 even at the higher pyrolysis temperature (850 °C), which meant that nano-Fe could accelerate the conversion of amorphous carbon to graphitic carbon in the adsorbent at the appropriate pyrolysis temperature (see Fig. S1 in the ESI†). In addition, two Raman bands called 2D and D + G located at 2500–3100 cm^{-1} were observed from the spectra. The 2D band is ascribed to active crystalline graphitic carbon, and it is sensitive to the π-band in the graphitic electronic structure, while the combination mode of D + G is induced by disordered carbon.[47] The peak strength of the 2D band increased significantly with increasing pyrolysis temperature from 750 °C to 950 °C, which indicated that high pyrolysis temperature is conducive to the formation of graphitic carbon. As shown in Fig. S1,† no 2D band peak was observed from the spectra of C-850, which further confirmed the acceleration of nano-Fe for the graphitization of porous carbon adsorbent.[48]

The 77 K N_2 physical adsorption–desorption method was employed to determine the pore structure and specific

surface area of Fe–C composites (Fig. S2a and Tables S1 and S2†). The specific surface area of the tested Fe–C composites was determined to be 306.37 $m^2 g^{-1}$ (Fe–C-500), 348.28 $m^2 g^{-1}$ (Fe–C-600), 361.30 $m^2 g^{-1}$ (Fe–C-750), 338.12 $m^2 g^{-1}$ (Fe–C-850) and 326.20 $m^2 g^{-1}$ (Fe–C-950). According to the adsorption–desorption isotherms of Fe–C-500 and Fe–C-650, a typical type IV isotherm with H4 hysteresis was observed, which meant that the adsorbent was composed of micropores and mesopores and contained a large number of narrow and fractured pores. With further increasing the pyrolysis temperature, the hysteresis loop of Fe–C adsorbents changed from H4 to H1, indicating that high-temperature carbon reconstruction can promote the formation of the mesoporous structure of Fe–C adsorbents. For instance, when the temperature increased from 600 °C to 850 °C, the proportion of micropores decreased from 51% to 24%, while the proportion of mesopores increased from 42% to 68%. That is, an obvious carbon-reforming effect occurs inside the adsorbents in this temperature range (Fig. 2c). As compared with our previous report, this result suggested that the pore structure of carbon adsorbents could be significantly improved by nano-Fe particles, and higher specific surface area, pore volume, and mesoporous ratio were obtained even at lower pyrolysis temperature.[15] These results were very consistent with XRD and Raman analysis results.

The various functional groups of the Fe–C composites were analysed by combining FT-IR and Boehm's titration method. As shown in Fig. 2d and Table S3,† the total concentration of oxygen-containing functional groups in Fe–C composites was calculated to be 5.082 μmol g^{-1} (Fe–C-500), 5.095 μmol g^{-1} (Fe–C-600), 4.582 μmol g^{-1} (Fe–C-750), 3.398 μmol g^{-1} (Fe–C-850) and 4.279 μmol g^{-1} (Fe–C-950). Except for the lactonic group, the concentrations of the carboxylic group, phenolic group, and basic group all showed an obvious decrease at 850 °C. Combined with FT-IR spectra (Fig. S3†), when the pyrolysis temperature gradually increased from 500 °C to 950 °C, C–O or C–OH functional groups were gradually decreased in the range of 940–1220 cm^{-1}, and the C=O and aromatic C–H stretching located at 1693 cm^{-1} and 877 cm^{-1} almost disappeared. The above results indicated that the internal transformation of major functional groups occurs when oxygen-containing functional groups fall off (such as the increase of the lactonic group). In addition, the Fe element also led to the uncertainty change of functional groups at the interface (such as the first decrease and then increase of the carboxylic group, phenolic group, and basic group). In particular, aromatic C=C stretching located at 1602 cm^{-1} decreased significantly until it disappeared, which indicated that the pyrolysis process not only involved dehydration and condensation reactions but also promoted the catalytic reconstruction of porous carbon structure and the formation of graphitic carbon structure.[49,50]

In order to investigate the effect of the presence of the Fe component on the decomposition of the organic carbon matrix, TG-DSC of the organic dry gels was carried out under argon protection (Fig. S4†). The weight loss of about 4.08–4.38% at the range of 30–120 °C was assigned to the desorption of adsorbed water. Although obvious weight loss occurs at 250 °C to 600 °C for the pure carbon gel precursor, the overall endothermic and exothermic peaks were relatively gentle, indicating that the pyrolysis reaction and carbon reconfiguration reaction inside the carbon gel were relatively mild. For the Fe–C composite gel precursor, there was not only an obvious endothermic process at 120–300 °C but also an obvious endothermic peak and exothermic peak near 315 °C and 350 °C. In addition, the Fe–C composite gel precursor has a violent exothermic peak after 370 °C, which indicates that the Fe–C composite has undergone a violent solid phase reaction. The graphitization transformation of amorphous carbon and the reconstruction of pore structure are also realized in this process.

3.3 Adsorption and regeneration performance

The adsorption and regeneration behaviors of Fe–C adsorbents were conducted using a fixed-bed adsorption–desorption system equipped with a gas-distributing system providing the gaseous VOCs (ethyl acetate, EA, toluene) operating in a continuous flow-through mode. The adsorption capacity of Fe–C adsorbents with different Fe/C molar ratios are given in Fig. S5.† The highest adsorption capacity (153 mg g^{-1}) of EA was obtained when the Fe/C molar ratio was 1 : 20. This is because a higher proportion of Fe component will lead to the formation of large iron oxide particles, which is not conducive to the reconstruction of carbon skeleton structure, and may block the pore structure. Appropriate Fe content could achieve better carbon reconstruction, which significantly enhanced the adsorption capacity of EA.[51] Hence, Fe–C composites with the optimum Fe/C molar ratio (1 : 20) were selected and pyrolyzed under different temperatures, and the adsorption trends of the obtained adsorbents for EA and toluene are shown in Fig. 3a. The proportions of the actual Fe element in these adsorbents were also calculated based on the results of ICP-MS. The best adsorption performance for EA (average adsorption capacity: 151 mg g^{-1}) and toluene (average adsorption capacity: 208 mg g^{-1}) are observed in Fe–C-600 and Fe–C-750, respectively, which was mainly attributed to the high specific surface area (348 $m^2 g^{-1}$ and 361 $m^2 g^{-1}$) and pore volume (0.20 mL g^{-1} and 0.22 mL g^{-1}) of the two adsorbents. Combined with the XRD and Raman results, the high degree of graphitization seemed to be more conducive for the toluene adsorption, which was mainly attributed to the π–π stacking of the benzene ring structure in graphitic carbon.[2] The reason why Fe–C-600 possessed a high EA adsorption capacity with the maximum probability was because of its high micropore volume (0.1 mL g^{-1}) and the coordination adsorption of nanometer Fe.[52]

The regenerated adsorption properties of two optimal adsorbents for EA and toluene were further investigated, and the results are given in Fig. 3b. Interestingly, the regenerated adsorption capacity of both adsorbents reached 100% after five cycles, which displayed a significant improvement over

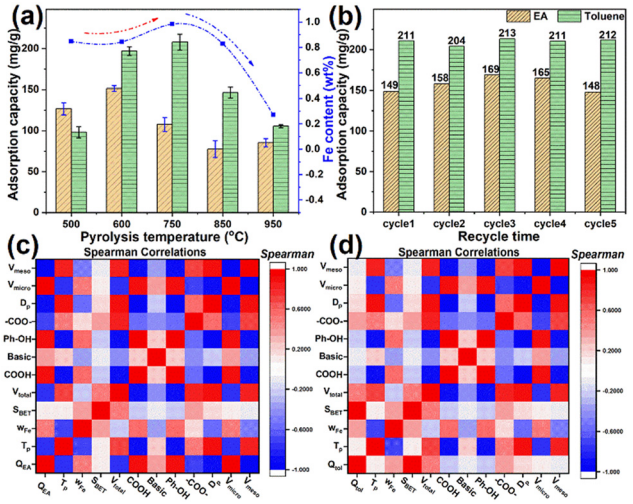

Fig. 3 Adsorption capacity (a) and regenerated adsorption capacity (b) of EA and toluene over Fe–C composites prepared at different pyrolysis temperatures. Spearman correlations of EA (c) and toluene (d) adsorption capacity with pore structure, functional groups, and other factors.

the pure carbon adsorbents (only 80%) as compared with our previous report.[15] In other words, the presence of the nano-Fe component could significantly promote the regeneration of porous carbon adsorbents and maintain their stable regeneration adsorption capacity, which is of great significance for the recovery of industrial VOC exhaust gas. In order to further confirm the contribution of nano-iron on adsorbent regeneration, the time–temperature variation and infrared thermography of Fe–C-600, Fe–C-750, and C-750 were conducted and given in Fig. S6–S9.† It was noted that the actual temperature of the Fe–C adsorbent was higher than that of the C-750 adsorbent at a lower temperature range (≤120 °C). The rapid growth range of actual temperature was 105.1–106.8 °C, 107.8–108.0 °C, and 102.5–117.8 °C, and the corresponding time required was 13 s, 0.2 s, and 16 s, respectively. These results indicated that Fe–C adsorbents had better thermal conductivity than C-750, especially Fe–C-750 adsorbents, which could be attributed to the higher heat transfer efficiency of nano-iron and graphitic carbon. Usually, the faster thermal conductivity efficiency will reduce the residence time of VOCs on the interface, thus reducing the probability of VOC thermochemical reaction.[53]

To further investigate the contribution of key factors to adsorption capacity, the Spearman correlation coefficient between the adsorption capacity and the pore structure, functional groups, and other factors was calculated and shown in Fig. 3c and d and Tables S4 and S5.† For EA adsorption, the influencing factors with positive correlation were determined as micropore volume (1.00), carboxyl group (0.90), phenolic hydroxyl group (0.90), mass fraction of Fe element (0.50), base groups (0.36) and specific surface area (0.10). The results showed that the pore volume of micropores and some oxygen-containing groups contributed significantly to the increase of the EA adsorption capacity, which was mainly due to the larger capacity of the adsorbent and the electrostatic attraction (such as hydrogen bonding) of functional groups.[2,54] In addition, the proportion of actual Fe element in the two adsorbents is at a high level of 0.84% and 0.98%, respectively. EA adsorption could also be promoted by the coordination effect of the Fe component at the interface of the Fe–C adsorbent. For toluene adsorption, the key influencing factors such as specific surface area (1.00), total pore volume (0.50), mass fraction of Fe element (0.40), lactonyl group (0.40), pore diameter (0.20), pore volume of micropores (0.10) and pyrolysis temperature (0.10) were calculated based on Spearman correlation analysis. There is a significant positive correlation between the specific surface area of the Fe–C adsorbent and the adsorption capacity of toluene. It is obvious that a large specific surface area can provide sufficient adsorption active sites for toluene adsorption. In addition, the total pore volume, mass fraction of Fe element, lactonyl group, and so on have a certain weak positive correlation with the adsorption capacity of toluene. On the one hand, it could be attributed to the high accommodating volume of the adsorbent for toluene molecular structure; on the other hand, the optimization of the pore structure and interface structure of the adsorbent by nano-Fe could effectively improve the pore accessibility of toluene and greatly increase the effective active site of the Fe–C adsorbent.

3.4 *In situ* DRIFTS analysis

In order to investigate the adsorption mechanism of EA on Fe–C adsorbents, *in situ* DRIFTS experiments were carried out and shown in Fig. 4. When EA was introduced into the IR cell at 10 min, some typical peaks of 1734 cm^{-1}, 1371 cm^{-1}, 1252 cm^{-1}, 1240 cm^{-1} and 1039 cm^{-1} were observed from the spectra of Fe–C adsorbents. Therein, 1734 cm^{-1} represented the signal of C=O of EA; 1371 cm^{-1} belonged to the C–H of methyl species; the peaks located at 1252 cm^{-1}, 1240 cm^{-1}, 1053 cm^{-1} and 1039 cm^{-1} were assigned to C–O–C.[19] The peak of 1734 cm^{-1} was only observed on Fe–C-500, Fe–C-600, and C-600 with low graphitization, among which Fe–C-500 had the most significant peak intensity, followed by Fe–C-

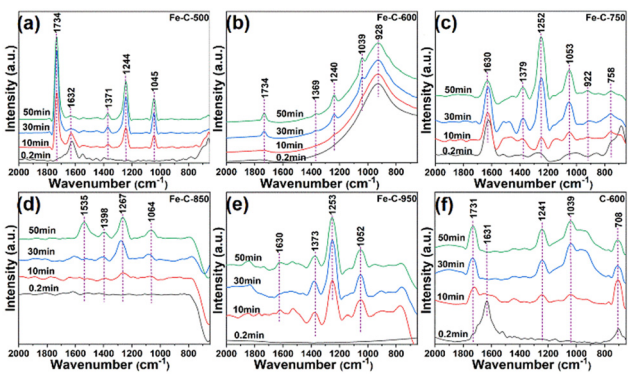

Fig. 4 Time-dependent *in situ* DRIFTS of EA adsorption over Fe–C adsorbents: (a) Fe–C-500, (b) Fe–C-600, (c) Fe–C-750, (d) Fe–C-850, (e) Fe–C-950, and (f) C-600.

600, and no reflection peak was observed on other Fe–C adsorbents with high graphitization. Although Fe–C-500 and Fe–C-600 adsorbents had a lower specific surface area, they had a higher EA adsorption capacity than other Fe–C adsorbents with high specific surface area, suggesting the high contribution of oxygen-containing groups to EA adsorption. Besides, some typical peaks near 1252 cm^{-1} and 1053 cm^{-1} assigned to C–O–C of EA were observed on Fe–C-750–950 with high graphitization. That is, the adsorption patterns of EA on low graphitized adsorbents (such as Fe–C-500 and Fe–C-600) are significantly different from those on high graphitized adsorbents (such as Fe–C-750, Fe–C-850 and Fe–C-950). For adsorbents with high oxygen functional groups, EA is more inclined to bind to the adsorbent interface with carbonyl bonds, while for high graphitized adsorbents, EA is more inclined to bind to the adsorbent interface with ether bonds. This was because abundant oxygen-containing functional groups acted as electron donors or acceptors to establish a donor–acceptor mechanism through hydrogen-bond interaction.[17] These results indicated that the electrostatic attraction of oxygen-containing functional groups could significantly promote the adsorption process of EA.

Similarly, the possible adsorption forms of toluene on Fe–C adsorbents were also investigated by *in situ* DRFITs and shown in Fig. 5. Some typical peaks around 1630 cm^{-1} and 1520 cm^{-1}, 1377–1389 cm^{-1} and 717–735 cm^{-1} were observed on the spectra of Fe–C adsorbents, which were assigned to the C=C, C–H of $-CH_3$ of toluene and C–H of the benzene ring. For the C-750 adsorbent, only a distinct peak of the C=C bond near 1630 cm^{-1} was observed. It was found that there were multiple adsorption modes between Fe–C adsorbents and toluene as compared with pure carbon adsorbent, including π–π stacking, the electrostatic interaction between C–H and the interface on the benzene ring, and the electrostatic interaction on the substituted methyl group, which was mainly due to the diversified pore structure and interfacial functional groups of the Fe–C adsorbents. In the case of the optimal adsorbent Fe–C-750, the peak area at around 1627, 1518, 1389, and 735 cm^{-1} gradually increased with the increase of adsorption time; a significant peak area increase was observed at 1627 and 1518 cm^{-1}, suggesting that the π–π interaction between the hexagonal ring structure of the graphitic carbon on the Fe–C adsorbents and the aromatic ring of toluene was the dominant driving force for the toluene adsorption.[55] In addition, the feature peak located at 735 cm^{-1} (C–H of benzene ring) and 1382 cm^{-1} (C–H of $-CH_3$ of toluene) was another significant contribution of feature peak area, indicating that the electrostatic interaction between the C–H group of toluene and the adsorption interface was another main driving force for the toluene adsorption.[56] In conclusion, the diverse pore structure and rich functional groups of Fe–C adsorbents are key factors for enhancing the physical and chemical adsorption of Fe–C adsorbents, resulting in obtaining high adsorption capacity of toluene.

3.5 Adsorption and regeneration mechanism of Fe–C adsorbents

To further explore the reasons for the high regenerated adsorption capacity of Fe–C adsorbent, the composition and functional groups of the Fe–C adsorbents before and after the regeneration were determined by XPS semiquantitative analysis method. For EA recycling, the C, O, and Fe composition of Fe–C-600 was determined by deconvolution of XPS spectra (see Fig. S10 in the ESI†). The C 1s spectrum was deconvoluted into sub-peaks located at 284.8, 286.4, 287.9, and 289.6 eV, which were assigned to C=C, C–OH, C–O, and C=O, respectively. The O 1s spectrum was deconvoluted into sub-peaks located at 530.6, 532.3, and 533.8 eV, which were assigned to C=O, O=C–O–(C, O), and C–O–C, respectively. The deconvoluted peaks located at 724.6 and 711.7 eV were assigned to Fe $2p_{1/2}$ and Fe $2p_{3/2}$. After five regeneration cycles, the total C proportion decreased from 85.29% to

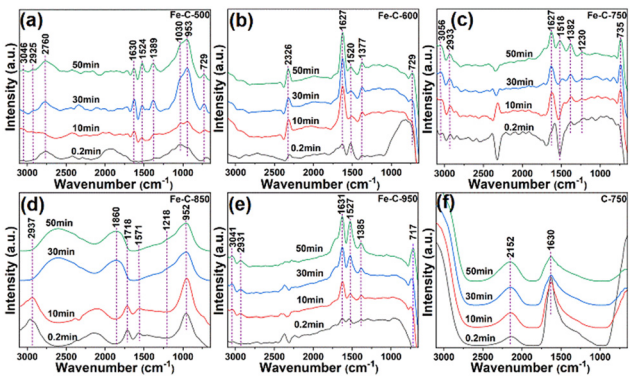

Fig. 5 Time-dependent *in situ* DRIFTS of toluene adsorption over Fe–C synthesized at different pyrolysis temperatures. (a) Fe–C-500, (b) Fe–C-600, (c) Fe–C-750, (d) Fe–C-850, (e) Fe–C-950, and (f) C-750.

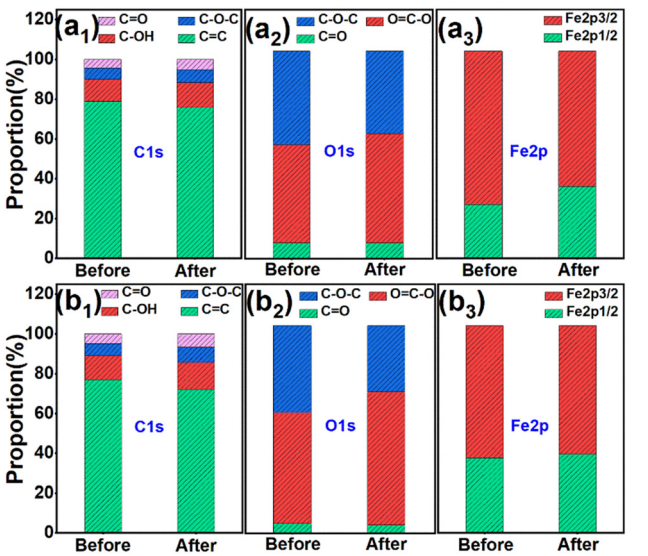

Fig. 6 Proportion of functional groups on Fe–C-600 (a_1–a_3) and Fe–C-750 (b_1–b_3) by deconvolution of XPS C 1s, O 1s and Fe 2p spectra before and after recycling.

80.34%, and the total proportion of O and Fe composition increased from 13.42% and 1.29% to 17.16% and 2.5% (Fig. 6a_1–a_3 and Table S6†). Among them, the increase in total O was mainly due to the increase of O═C–O–(C, O), which was mainly attributed to the chemical coupling structure formed between EA and the adsorption sites during the heat treatment process. The increase of total Fe components indicated that nano-Fe could promote the desorption of amorphous carbon or impurity carbon around the Fe site, thereby reducing the formation of carbonaceous species with high carbon components and effectively avoiding the deactivation of adsorbents.

For toluene recycling, the proportion of functional groups on Fe–C-750 was determined by XPS C 1s, O 1s, and Fe 2p spectra (see Table S7 and Fig. S11 in the ESI†). Different from EA recycling, the total C proportion increased from 81.08% to 88.11%, and the total proportion of O and Fe composition decreased from 17.57% and 11.14% to 1.35% and 0.75% (Fig. 6b_1–b_3). It was speculated that a very small amount of toluene was chemically coupled to the adsorption sites or a thermochemical reaction had occurred. However, from the 100% regenerated adsorption capacity of Fe–C-750 and the significant reduction of oxygen-containing groups, there was no obvious thermochemical reaction in the toluene cycle, but only a simple chemical adsorption. In other words, the presence of nano-Fe components not only enhanced the chemisorption of toluene to a certain extent but also promoted the drop of oxygen-containing carbon groups at the interface of the Fe–C adsorbent to avoid further thermochemical reactions, thus effectively inhibiting the deactivation process of the adsorbent.

Based on the above results, the enhanced adsorption and regeneration mechanism was discussed and shown in Fig. 7. The heel build-up was generally formed on porous carbon adsorbents after repeated adsorption and regeneration limited by its single pore structure and non-adjustable functional groups, resulting in a gradual decline in adsorption capacity of the regenerated adsorbent until it was deactivated. Interestingly, by introducing nano-Fe components, the degree of graphitization and porous channel structure of the adsorbents were greatly improved by the effect of *in situ* catalytic carbon restructuring during the preparation process, which would provide a diversified diffusion channel for promoting the adsorption and desorption of VOC molecules. Abundant nano-Fe sites and oxygen-containing groups could establish a donor–acceptor adsorption mechanism with EA and toluene to enhance the chemisorption. In addition, many nano-iron sites and graphitic carbon structures made the pore structure of Fe–C adsorbents have higher heat transfer efficiency. Therefore, the Fe–C adsorbent integrated many of the above advantages so that it not only possessed a high adsorption capacity but also a rapid desorption diffusion of VOCs could be achieved with the help of diversified diffusion channels and thermal effect sites during the thermal desorption process. High desorption diffusion of VOCs was beneficial for inhibiting the thermal activation reaction between VOC molecules and the active sites of the adsorbent, and almost no heel build-up was formed, resulting in high regeneration efficiency of Fe–C adsorbents as compared with previous reports (Table S8†).

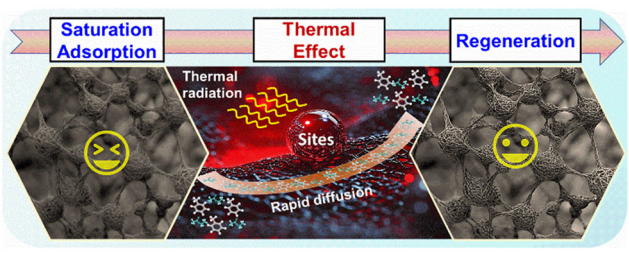

Fig. 7 Schematic diagram of adsorption and regeneration on Fe–C adsorbents for VOC recycling.

Conclusions

The deactivation of porous carbon adsorbents is a big limitation for the resource utilization or control of industrial VOC waste gas. Multifunctional Fe/FeO_x/NPC adsorbents were synthesized by an *in situ* reconstruction method using nano-Fe as a catalyst. Fe–C adsorbents showed high adsorption capacity for toluene and EA and regeneration efficiency without deactivation after five adsorption–regeneration cycles. Spearman correlation analysis and *in situ* DRIFTS analysis showed that the synergistic effect of interfacial active sites, including nano-Fe sites and diverse pore structures, could significantly improve the adsorption strength and capacity of VOC molecules at the interface of the Fe–C adsorbent. The abundant thermal effect sites in the pore structure could also accelerate the desorption diffusion mass transfer of VOCs and greatly reduce the formation of heel build-up. Although this study focuses on the high regeneration efficiency of Fe/FeO_x/NPC for the adsorption and regeneration of toluene and ethyl acetate, whether it is equally applicable to other types of VOCs requires further study and verification, particularly its ability to resist physical and chemical deactivation under continuous use and varying operational conditions.

Data availability

Data available on request from the authors. The data that support the findings of this study are available from the corresponding author (W. P. Zhang) upon reasonable request.

Author contributions

Weiping Zhang performed conceptualization, funding acquisition, project administration, writing – review & editing and supervised the findings of this work. Xiong Xiao and Xiaoqin Wang conducted experiments, data analysis and wrote the original manuscript. Hongli Liu contributed to the investigation of the main content. Xingye Zeng verified the analytical methods. Taicheng An contributed significantly to conceptualization, manuscript preparation and review.

Conflicts of interest

There are no conflicts to declare.

Acknowledgements

The authors acknowledge the National Key Research & Development Program of China (2024YFE0110800, 2023YFC3708203, 2023YFC3708204), the National Natural Science Foundation of China (42477411 and 22076028), the Local Innovative and Research Teams Project of Guangdong Pearl River Talents Program (2017BT01Z032), and the Guangdong Basic and Applied Basic Research Foundation (2024A1515013253). Many thanks to Xian Qiu, who helped to improve the language accuracy and coherence of our essay.

Notes and references

1 M. Simayi, Y. Shi, Z. Xi, J. Ren, G. Hini and S. Xie, Emission trends of industrial VOCs in China since the clean air action and future reduction perspectives, *Sci. Total Environ.*, 2022, **826**, 153994.

2 W. Zhang, G. Li, H. Yin, K. Zhao, H. Zhao and T. An, Adsorption and desorption mechanism of aromatic VOCs onto porous carbon adsorbents for emission control and resource recovery: recent progress and challenges, *Environ. Sci.: Nano*, 2022, **9**, 81–104.

3 F. Yang, L.-a. Xing, X. Zhong, Y. Liu, Z. Guo, J. Yang, A. Yuan and J. Pan, Volatile acetic acid selective adsorption by biomass-derived activated carbon with humidity-resistance: Tunable implanting and activation approach of activator, *Sep. Purif. Technol.*, 2024, **341**, 126891.

4 T. Moufawad, M. Costa Gomes and S. Fourmentin, Deep eutectic solvents as absorbents for VOC and VOC mixtures in static and dynamic processes, *Chem. Eng. J.*, 2022, **448**, 137619.

5 K.-H. Lee, C. Yeom and J. Kim, Separation recovery of dilute organics from aqueous solution by membrane distillation and selective condensation hybrid process, *Sep. Purif. Technol.*, 2022, **300**, 121813.

6 G. Gan, S. Fan, X. Li, Z. Zhang and Z. Hao, Adsorption and membrane separation for removal and recovery of volatile organic compounds, *J. Environ. Sci.*, 2023, **123**, 96–115.

7 J. Kong, S. Song, W. Zhao, Z. Yu, Z. Xiang, G. Li, W. Zhang and T. An, Unraveling a trade-off between positive effect and poisoning mechanism of soot over low-dose $PtCu/CeO_2$ for simultaneously photothermocatalytic removal of VOCs and soot, *Appl. Catal., B*, 2023, **339**, 123118.

8 S. H. Liu and W. X. Lin, A simple method to prepare g-C_3N_4-TiO_2/waste zeolites as visible-light-responsive photocatalytic coatings for degradation of indoor formaldehyde, *J. Hazard. Mater.*, 2019, **368**, 468–476.

9 H. Liu, X. Chang, X. Liu, G. Li, W. Zhang and T. An, Boosting the photocatalytic degradation of ethyl acetate by a Z-scheme Au–TiO_2@NH_2-UiO-66 heterojunction with ultrafine Au as an electron mediator, *Environ. Sci.: Nano*, 2021, **8**, 2542–2553.

10 Z. He, J. Li, J. Chen, Z. Chen, G. Li, G. Sun and T. An, Treatment of organic waste gas in a paint plant by combined technique of biotrickling filtration with photocatalytic oxidation, *Chem. Eng. J.*, 2012, **200–202**, 645–653.

11 L. Zhu, D. Shen and K. H. Luo, A critical review on VOCs adsorption by different porous materials: Species, mechanisms and modification methods, *J. Hazard. Mater.*, 2020, **389**, 122102.

12 H. Liu, M. Xu, G. Li, W. Zhang and T. An, Solar-light-triggered regenerative adsorption removal of styrene by silver nanoparticles incorporated in metal–organic frameworks, *Environ. Sci.: Nano*, 2021, **8**, 543–553.

13 M. R. Benzigar, S. N. Talapaneni, S. Joseph, K. Ramadass, G. Singh, J. Scaranto, U. Ravon, K. Al-Bahily and A. Vinu, Recent advances in functionalized micro and mesoporous carbon materials: synthesis and applications, *Chem. Soc. Rev.*, 2018, **47**, 2680–2721.

14 W. Xiang, X. Zhang, K. Chen, J. Fang, F. He, X. Hu, D. C. W. Tsang, Y. S. Ok and B. Gao, Enhanced adsorption performance and governing mechanisms of ball-milled biochar for the removal of volatile organic compounds (VOCs), *Chem. Eng. J.*, 2020, **385**, 123842.

15 W. Zhang, X. Wang, H. Pan, X. Zeng, G. Li, H. Liu, J. Kong, H. Zhao and T. An, Experimental and DFT investigations on adsorption–regeneration performance and deactivation mechanism over engineered carbon fiber: role of pore structure and functional groups, *Environ. Sci.: Nano*, 2023, **10**, 2790–2798.

16 X. Zhang, B. Gao, A. E. Creamer, C. Cao and Y. Li, Adsorption of VOCs onto engineered carbon materials: A review, *J. Hazard. Mater.*, 2017, **338**, 102–123.

17 X. Li, L. Zhang, Z. Yang, P. Wang, Y. Yan and J. Ran, Adsorption materials for volatile organic compounds (VOCs) and the key factors for VOCs adsorption process: A review, *Sep. Purif. Technol.*, 2020, **235**, 116213.

18 G. Ye, Y. Wang, W. Zhu, X. Wang, F. Yao, Y. Jiao, H. Cheng, H. Huang and D. Ye, Preparing hierarchical porous carbon with well-developed microporosity using alkali metal-catalyzed hydrothermal carbonization for VOCs adsorption, *Chemosphere*, 2022, **298**, 134248.

19 H. Liu, N. Li, M. Feng, G. Li, W. Zhang and T. An, Near-infrared light induced adsorption–desorption cycle for VOC recovery by integration of metal–organic frameworks with graphene oxide nanosheets, *Environ. Sci.: Nano*, 2022, **9**, 1858–1868.

20 H. Zhang, Z. Yang, E. Cao, Y. Zheng, Q. Ren and Y. Cui, Direct activation and hydrophobic modification of biomass-derived hierarchical porous carbon for toluene adsorption under high humidity, *Chem. Eng. J.*, 2024, **490**, 151817.

21 Y. Guo, C. Su, H. Chen, J. Wang, B. Liu, Z. Zeng and L. Li, Hierarchical porous carbon with tunable apertures and nitrogen/oxygen heteroatoms for efficient adsorption and separation of VOCs, *Chem. Eng. J.*, 2023, **471**, 144558.

22 G. Wang, B. Dou, Z. Zhang, J. Wang, H. Liu and Z. Hao, Adsorption of benzene, cyclohexane and hexane on ordered mesoporous carbon, *J. Environ. Sci.*, 2015, **30**, 65–73.

23 L. Li, Y. Lv, J. Wang, C. Jia, Z. Zhan, Z. Dong, L. Liu and X. Zhu, Enhance pore structure of cyanobacteria-based porous

carbon by polypropylene to improve adsorption capacity of methylene blue, *Bioresour. Technol.*, 2022, **343**, 126101.

24 M. Jahandar Lashaki, Z. Hashisho, J. H. Phillips, D. Crompton, J. E. Anderson and M. Nichols, Mechanisms of heel buildup during cyclic adsorption-desorption of volatile organic compounds in a full-scale adsorber-desorber, *Chem. Eng. J.*, 2020, **400**, 124937.

25 S. Niknaddaf, J. D. Atkinson, P. Shariaty, M. Jahandar Lashaki, Z. Hashisho, J. H. Phillips, J. E. Anderson and M. Nichols, Heel formation during volatile organic compound desorption from activated carbon fiber cloth, *Carbon*, 2016, **96**, 131–138.

26 M. Jahandar Lashaki, J. D. Atkinson, Z. Hashisho, J. H. Phillips, J. E. Anderson and M. Nichols, The role of beaded activated carbon's pore size distribution on heel formation during cyclic adsorption/desorption of organic vapors, *J. Hazard. Mater.*, 2016, **315**, 42–51.

27 M. Feizbakhshan, Z. Hashisho, D. Crompton, J. E. Anderson and M. Nichols, Effect of activated carbon's pore size distribution on oxygen induced heel build-up, *J. Hazard. Mater.*, 2023, **457**, 126905.

28 M. Jahandar Lashaki, J. D. Atkinson, Z. Hashisho, J. H. Phillips, J. E. Anderson and M. Nichols, The role of beaded activated carbon's surface oxygen groups on irreversible adsorption of organic vapors, *J. Hazard. Mater.*, 2016, **317**, 284–294.

29 S. Mojtaba Hashemi, M. Jahandar Lashaki, Z. Hashisho, J. H. Phillips, J. E. Anderson and M. Nichols, Oxygen impurity in nitrogen desorption purge gas can increase heel buildup on activated carbon, *Sep. Purif. Technol.*, 2019, **210**, 497–503.

30 S. Niknaddaf, J. D. Atkinson, A. Gholidoust, M. Fayaz, R. Awad, Z. Hashisho, J. H. Phillips, J. E. Anderson and M. Nichols, Influence of Purge Gas Flow and Heating Rates on Volatile Organic Compound Decomposition during Regeneration of an Activated Carbon Fiber Cloth, *Ind. Eng. Chem. Res.*, 2020, **59**, 3521–3530.

31 F. Meng, M. Song, Y. Wei and Y. Wang, The contribution of oxygen-containing functional groups to the gas-phase adsorption of volatile organic compounds with different polarities onto lignin-derived activated carbon fibers, *Environ. Sci. Pollut. Res.*, 2019, **26**, 7195–7204.

32 M. Davarpanah, Z. Hashisho, D. Crompton, J. E. Anderson and M. Nichols, Modeling VOC adsorption in lab- and industrial-scale fluidized bed adsorbers: Effect of operating parameters and heel build-up, *J. Hazard. Mater.*, 2020, **400**, 123129.

33 Y.-T. Chen, Y.-P. Huang, C. Wang, J.-G. Deng and H.-C. Hsi, Comprehending adsorption of methylethylketone and toluene and microwave regeneration effectiveness for beaded activated carbon derived from recycled waste bamboo tar, *J. Air Waste Manage. Assoc.*, 2020, **70**, 616–628.

34 J. Cai, D. Wang, M. Zhang, H. Sui, X. Li and L. He, Deactivation Mechanisms of Engineering Adsorbents for VOCs Adsorption and the Lifetime-Prolonging Strategy, *Ind. Eng. Chem. Res.*, 2022, **61**, 5952–5962.

35 A. Bhat, M. Venkat, X. Chen, H. Ohtani, K. Ellwood, T. Misovski and J. W. Schwank, Chemical surface modification of beaded activated carbon: A strategy to inhibit heel accumulation from VOC, *J. Ind. Eng. Chem.*, 2021, **103**, 205–215.

36 M. Jahandar Lashaki, S. Kamravaei, Z. Hashisho, J. H. Phillips, D. Crompton, J. E. Anderson and M. Nichols, Adsorption and desorption of a mixture of volatile organic Compounds: Impact of activated carbon porosity, *Sep. Purif. Technol.*, 2023, **314**, 123530.

37 S. Joo, A. Seong, O. Kwon, K. Kim, J. H. Lee, R. J. Gorte, J. M. Vohs, J. W. Han and G. Kim, Highly active dry methane reforming catalysts with boosted in situ grown Ni-Fe nanoparticles on perovskite via atomic layer deposition, *Sci. Adv.*, 2020, **6**, eabb1573.

38 L. Zhou, J. M. P. Martirez, J. Finzel, C. Zhang, D. F. Swearer, S. Tian, H. Robatjazi, M. Lou, L. Dong, L. Henderson, P. Christopher, E. A. Carter, P. Nordlander and N. J. Halas, Light-driven methane dry reforming with single atomic site antenna-reactor plasmonic photocatalysts, *Nat. Energy*, 2020, **5**, 61–70.

39 Y. Li, Z. Xu, J. Wang, B. Wang and T. Zhu, Decomposition mechanism of Cl-VOCs on Cu- and Fe-modified activated carbon in an O_2-free atmosphere: The oxidation pathway and product distribution, *Sep. Purif. Technol.*, 2024, **334**, 125969.

40 H. Wu, Q. Ai, C. Yang, R. Huang, G. Jiang, J. Xiong and S. Yuan, Preparation and electrochemical properties of Fe/Fe_3O_4@r-GO composite nanocage with 3D hollow structure, *J. Solid State Electrochem.*, 2020, **25**, 869–879.

41 J. Cheng, S. Niu, M. Kang, Y. Liu, F. Zhang, W. Qu, Y. Guan and S. Li, The thermal behavior and flame retardant performance of phase change material microcapsules with modified carbon nanotubes, *Energy*, 2022, **240**, 122821.

42 W. Zhang, G. Li, H. Liu, J. Chen, S. Ma and T. An, Micro/nano-bubble assisted synthesis of Au/TiO_2@CNTs composite photocatalyst for photocatalytic degradation of gaseous styrene and its enhanced catalytic mechanism, *Environ. Sci.: Nano*, 2019, **6**, 948–958.

43 B. Li, H. Xiong, Y. Xiao, J. Hu, X. Zhang, L. Li and R. Wang, Efficient Toluene Adsorption on Metal Salt-Activated Porous Carbons Derived from Low-Cost Biomass: A Discussion of Mechanism, *ACS Omega*, 2020, **5**, 13196–13206.

44 Y. Wang, Z. Li, C. Tang, H. Ren, Q. Zhang, M. Xue, J. Xiong, D. Wang, Q. Yu, Z. He, F. Wei and J. Jiang, Few-layered mesoporous graphene for high-performance toluene adsorption and regeneration, *Environ. Sci.: Nano*, 2019, **6**, 3113–3122.

45 H. Li, X. Zhou, T. Wang, J. Wang, Y. Zhang and W.-P. Pan, Microporous three dimensional ordered zeolite-templated carbon for efficient removal of VOCs: Experimental study and molecular dynamics simulation, *Fuel*, 2023, **334**, 126849.

46 Z. Jankovská, L. Matějová, J. Tokarský, P. Peikertová, M. Dopita, K. Gorzolková, D. Habermannová, M. Vaštyl and J. Bělík, Microporous carbon prepared by microwave pyrolysis of scrap tyres and the effect of K^+ in its structure on xylene adsorption, *Carbon*, 2024, **216**, 118581.

47 W. Zhang, G. Li, H. Liu, J. Chen, S. Ma, M. Wen, J. Kong and T. An, Photocatalytic degradation mechanism of gaseous styrene over Au/TiO_2@CNTs: Relevance of superficial state with deactivation mechanism, *Appl. Catal., B*, 2020, **272**, 118969.

48 M. B. Vázquez-Santos, E. Geissler, K. László, J.-N. Rouzaud, A. Martínez-Alonso and J. M. D. Tascón, Graphitization of highly porous carbons derived from poly(p-phenylene benzobisoxazole), *Carbon*, 2012, **50**, 2929–2940.

49 R. D. Hunter, J. Ramírez-Rico and Z. Schnepp, Iron-catalyzed graphitization for the synthesis of nanostructured graphitic carbons, *J. Mater. Chem. A*, 2022, **10**, 4489–4516.

50 R. D. Hunter, M. Takeguchi, A. Hashimoto, K. M. Ridings, S. C. Hendy, D. Zakharov, N. Warnken, J. Isaacs, S. Fernandez-Muñoz, J. Ramirez-Rico and Z. Schnepp, Elucidating the Mechanism of Iron-Catalyzed Graphitization: The First Observation of Homogeneous Solid-State Catalysis, *Adv. Mater.*, 2024, **36**, 2404170.

51 W. Wu, K. Cheng, Y. Hu, H. He, P. Wang and C. Zhu, Adsorption and desorption mechanism of toluene gas by iron modified activated carbon fiber, *Chem. Phys.*, 2024, **580**, 112240.

52 K. Zhou, W. Ma, Z. Zeng, X. Ma, X. Xu, Y. Guo, H. Li and L. Li, Experimental and DFT study on the adsorption of VOCs on activated carbon/metal oxides composites, *Chem. Eng. J.*, 2019, **372**, 1122–1133.

53 M. Hu, S. Qing, X. Zhang, H. Zhang and Z. Shi, Thermal conductivity and photothermal characteristic of core-shell Fe_3O_4@C nanofluids in different particle size, *Powder Technol.*, 2024, **438**, 119631.

54 M. Ş. A. Eren, H. Arslanoğlu and H. Çiftçi, Production of microporous Cu-doped BTC (Cu-BTC) metal-organic framework composite materials, superior adsorbents for the removal of methylene blue (Basic Blue 9), *J. Environ. Chem. Eng.*, 2020, **8**, 104247.

55 K. Yang, J. Yang, Y. Jiang, W. Wu and D. Lin, Correlations and adsorption mechanisms of aromatic compounds on a high heat temperature treated bamboo biochar, *Environ. Pollut.*, 2016, **210**, 57–64.

56 W. Geng, S. Ge, X. He, S. Zhang, J. Gu, X. Lai, H. Wang and Q. Zhang, Volatile Organic Compound Gas-Sensing Properties of Bimodal Porous α-Fe_2O_3 with Ultrahigh Sensitivity and Fast Response, *ACS Appl. Mater. Interfaces*, 2018, **10**, 13702–13711.